PCCP

Accepted Manuscript

ROYAL SOCIETY OF CHEMISTRY

www.rsc.org/pccp

Physical Chemistry Chemical Physics
CREATED USING THE RSC LaTeX PCCP ARTICLE TEMPLATE – SEE www.rsc.org/electronicfiles FOR DETAILS
ARTICLE TYPE www. rsc.org/xxxxxx | XXXXXXXX

A hybrid density functional study on visible light photocatalytic activity of (Mo,Cr)-N codoped $KNbO_3$

Guangzhao Wang,[a] Hong Chen,*[a,b] Yang Li,[a] Anlong Kuang,[a] Hongkuan Yuan [a] and Gang Wu [a]

Received Xth XXXXXXXXXX 20XX, Accepted Xth XXXXXXXXX 20XX
First published on the web Xth XXXXXXXXXX 200X
DOI: 10.1039/b000000x

To improve the photocatalytic performance of $KNbO_3$ for the decomposition of water into hydrogen and oxygen, the electronic structure of $KNbO_3$ should be modified to own a suitable bandgap with band edge positions straddling the water redox level so as to sufficiently absorb visible light. Hybrid density functional theory has been used to calculate the electronic structures of pure, N, Mo, Cr monodoped, and Mo-N, Cr-N codoped $KNbO_3$. Especially, the influence of the relative positions of Mo-N or Cr-N codopants on the electronic structure of $KNbO_3$ is discussed in detail to account for the possible difference on the photocatalytic activity of the codoped samples prepared by different experimental techniques. The defect formation energy calculations indicate that N doped system is difficult to form under any condition and the codoped systems are energetically favorable under Nb-poor and O-rich conditions. It is interesting to find that the effective bandgap and stability for codoped systems decreases with the increase of the dopant concentration and/or the distance between dopants. Furthermore, the suitable bandgap and band edge position with respect to the water redox level make the Mo-N codoped systems good candidates for visible light photocatalytic decomposition of water to generate hydrogen.

1 Introduction

The semiconductor based photocatalyst has drawn much attention due to their potential applications in hydrogen energy industry and environmental pollution prevention[1–7]. Ideal photocatalyst must have proper band edge positions, that is to say, its valence band maximum (VBM) is lower than the oxygen evolution potential (OEP) and its conduction band minimum (CBM) is higher than the hydrogen evolution potential (HEP)[3]. Since TiO_2 was reported in 1972 to be used as photocatalyst for decomposition of water into H_2 and O_2[8], there has been great progress in photocatalytic decomposition of water in the ultraviolet light, many other metal oxide semiconductors such as ZnO, Cu_2O, $NaNbO_3$, $NaTaO_3$, $KTaO_3$, $BaTiO_3$, $SrTiO_3$, $SbNbO_4$, $SrTaO_4$, and $K_4Nb_6O_{17}$[9–17] have been found to have the ability to split water into O_2 and H_2 by using ultraviolet light. However, these materials which are limited by the wide bandgaps can only use ultraviolet light accounting for only 4% of solar energy, the development of photocatalytic materials which are sensitive to visible light is still challenging. To take full use of solar energy, the ideal photocatalyst should have bandgap around 2 eV so that it could use visible light which accounts for 43% of solar energy.

[a] *School of Physical Science and Technology, Southwest University, Chongqing 400715, People's Republic of China. E-mail: chenh@swu.edu.cn*
[b] *Key Laboratory of Luminescent and Real-Time Analytical Chemistry, Ministry of Education, College of Chemistry and Chemical Engineering, Southwest University, Chongqing 400715, People's Republic of China*

Doping with either metals[18–21] or nonmetals[22–27] has been demonstrated to be an effective way to reduce the bandgaps of semiconductors. Despite of the obvious enhancement of the visible light activity, monodoping does not significantly improve the photocatalytic efficiency. This could be attributed to the fact that monodoping with only donors or acceptors usually introduces partially occupied impurity states which act as electron-hole recombination centers and monodoping is usually accompanied with the spontaneous formation of compensating defects[28,29]. Many studies[30–36] have proved that employing codoping with both acceptors and donors is a promising way to modify the band structure of photocatalysts without the above-described problems appearing.

Perovskite-structured $KNbO_3$ which has the advantage of high stability and nontoxic has drawn much attention in the photocatalytic decomposition of water by using sunlight[37–41], but the wide bandgap of 3.14 eV[42] making $KNbO_3$ only sensitive to ultraviolet light limits its photocatalytic performance. Therefore, bandgap adjustment has to be performed on $KNbO_3$ so as to expand its light adsorption scope up to visible light with band edge positions straddling the water redox potential. Monodoping with different elements has been considered to adjust the band structure of $KNbO_3$. Recently, the theoretical study by Shen et al.[43] showed that the introduction of Cu in place of K atom for $KNbO_3$ crystal results in the peak of adsorption spectra shifting due to the high peak generated by Cu 3*d* states around the Fermi level. Later on, the experimental study by Lau et al.[44] showed that the N doped $KNbO_3$ nan-

otubes exhibit higher photocatalytic activity in photodegradation organic pollutants and photocatalytic water splitting under visible light region because of the narrower band gap (2.76 eV) as compared to that of pure $KNbO_3$ nanotubes. As described above, monodoping may limit the photocatalytic performance by introducing occupied impurity states acting as electron-hole recombination center. Besides, the charge imbalance leading to the formation of vacancies also suppress the photocatalytic efficiency by promoting trapping photogenerated charge carriers. So we try to reduce the bandgap of $KNbO_3$ to ideal value with higher CBM than HEP and lower VBM than OEP by employing a charge compensated codoping strategy. Monodoping with N which has higher $2p$ orbital energy than O $2p$ has been a suitable choice to reduce the bandgaps of many semiconductors by shifting the VBM upwards[45,46]. Besides, the VBM of $KNbO_3$ is much lower than the water oxidation potential, and introducing N into $KNbO_3$ is expected to narrow the bandgap. However, N doping is unfavorable in energy and introduces some located impurity states which limit the photocatalytic performance with promoting electron-hole recombination. Recent study shows that anion doping could be promoted by introducing cations[30], so substituting one Nb atom by a Mo or Cr atom which has one more valence electron will not only promote the N doping into $KNbO_3$ but also balance the charge. Furthermore, there are few studies on the photocatalytic activity of (Mo-N, Cr-N) codoped $KNbO_3$.

In this work, the effect of N, Mo, Cr monodoping and Mo-N, Cr-N atom pairs codoping on the electronic structure of $KNbO_3$ is discussed. Especially, three different configurations for Mo-N (or Cr-N) codoping are considered to explore the effect on photocatalytic ability of $KNbO_3$ caused by the relative doping positions of Mo (or Cr) and N atom and the effect on electronic structure of $KNbO_3$ by different doping concentrations is also discussed. Furthermore, the bandgap reduction and the characteristic changes of band edge positions are explained by analyzing the partial density of states. The defect binding energies for codoped systems are calculated to discuss the stability and the defect formation energies for all the doped systems are calculated to find the most suitable growth conditions. We also give the band edge positions with reference to the water redox potential. At last, the shift of optical absorption curves of codoped systems are displayed with respect to that of pure system.

2 Computational method and process

The first-principles calculations based on density functional theory (DFT) have been carried out to obtain the optimized geometry configurations by using Vienna ab initio simulation package (VASP) code[47,48] within Perdew-Burke-Ernzerhof (PBE) functional[49] under generalized gradient approximation

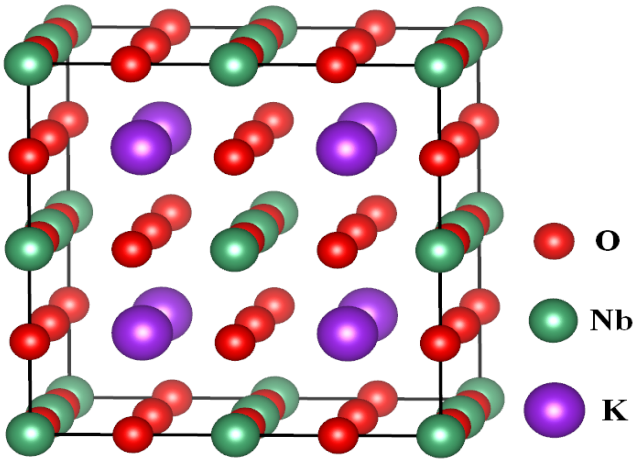

Fig. 1 2×2×2 supercell structure for pure $KNbO_3$.

(GGA)[50]. For geometry optimization, the Monkhorst-pack[51] k-point of 6×6×6 has been used and convergence thresholds for total energy has been set as 1.0×10^{-6} eV/atom with plane-wave cutoff energy of 400 eV. The higher plane-wave cutoff of 500 eV and k-points of 8×8×8 have also been tested for the geometry optimization of pure and doped systems, the difference of results is no more than 1%, so the calculated precisions we have described above are enough to treat the systems we considered. Because using GGA method seriously underestimates the bandgap value, the more time-consuming hybrid density functional as prescribed by Heyd-Scuseria-Ernzerhof (HSE)[52,53] has been adopted to accurately calculate the electronic structure including energy band structure, density of states (DOS), projected density of states (PDOS) and optical properties. The electron-electron interaction energy for HSE functional consists of short-ranged (SR) and long-ranged (LR) parts:

$$E_{XC}^{HSE} = \chi E_X^{SR}(\mu) + (1-\chi)E_X^{PBE,SR}(\mu) + E_X^{PBE,LR}(\mu) + E_C^{PBE}, \quad (1)$$

where μ is the screening parameter and χ is the mixing coefficient. In addition, the k-point of 3×3×3 has been set for hybrid density functional calculations. For all our calculations, the valence states of K ($3s^23p^64s^1$), Nb ($4p^65s^14d^4$), O ($2s^22p^4$), Mo ($4p^65s^14d^5$), Cr ($3p^63d^54s^1$) and N ($2s^22p^3$) have been treated for the construction of PAW potentials. By fitting the the experimental lattice constant and bandgap of pure $KNbO_3$, the μ and χ are determined as 0.20 Å $^{-1}$ and 0.30, respectively. For the $KNbO_3$ primitive cell, the optimized lattice constant of $a = b = c = 4.013$ Å is consistent with the experimental values of $a = b = c = 4.022$ Å[41] and the accurate bandgap of 3.01 eV is in good agreement with the experimental value of 3.14 eV[42], which indicates our calculations are reasonable and reliable.

The monodoped and codoped systems have been modeled with a relaxed 40-atoms supercell of perovskite-type $KNbO_3$ consisting of 12 K, 12 Nb and 24 O atoms, and the corresponding doping concentrations for monodoped and codoped systems are 2.5 at% and 5.0 at%, respectively. Substituting one Nb atom in the center of $KNbO_3$ supercell by a Mo or Cr atom is modeled to form cation doping and substituting the O atom adjacent to the center Nb atom by a N atom is considered to form anion doping. In order to discuss the effect caused by the relative positions of Mo (or Cr) atom and N atom on the electronic structure, three different Mo-N or Cr-N codoped configurations are considered: the Mo or Cr atom substitutes the Nb atom in the center of the supercell with (i) one N atom substituting the O atom adjacent to the Mo or Cr atom (the nearest configuration), (ii) one N atom substituting the O atom in the face of the cubic supercell (the next-nearest configuration), and (iii) one N atom substituting the O atom on the edge of the cubic supercell (the next-next-nearest configuration). In order to investigate the effect of the doping concentration on the electronic structure of $KNbO_3$, a larger $3\times2\times2$ supercell model with total of 60 atoms has been also considered in our calculation, which corresponds to the codoping concentration of 3.3 at%.

The defect binding energies have been calculated to discuss the relative stability of these codoped systems with respect to the pure system and the defect formation energies have been analyzed to find suitable growth conditions for different doped systems. The defect binding energy of X-N (X=Mo, N) codoped system could be calculated by

$$E_b = E(X) + E(N) - E(pure) - E(X+N), \tag{2}$$

where $E(pure)$, $E(X)$, $E(N)$, and $E(X+N)$ denote the total energies of pure, X doped, N doped, and X-N codoped $KNbO_3$ systems. The defect formation energy for $KNbO_3$ system carrying a charge of q with a defect or impurity X could be obtained by[56,57]

$$E_f(X^q) = E(X^q) - E(pure) - \sum_i n_i\mu_i + q(E_F + E_V + \Delta V). \tag{3}$$

The defect or impurity is formed by removing or adding n_i ($n_i < 0$ or $n_i > 0$) atoms of type i of chemical potential μ_i. The value of q is set as zero since we consider all the systems in neutral state. E_F is the Fermi level which is measured from the VBM of pure system (E_V). Since the formation of defects relates to the experimental growth or annealing environment, the defect formation energy depends on the chemical potentials of the host atoms reflected by the environment. When the pure system is in the equilibrium with the reservoirs of K, Nb and O atoms, the chemical potentials of K, Nb, and O atoms must be constrained by

$$\mu_K + \mu_{Nb} + 3\mu_O = \mu_{KNbO_3(bulk)}, \tag{4}$$

where $\mu_{KNbO(bulk)}$ is the chemical potential of the bulk $KNbO_3$, which is equal to the total energy of bulk $KNbO_3$ per primitive cell. μ_K, μ_{Nb}, and μ_O denoting the chemicals of K, Nb and O atoms are up to the chemical potentials of bulk K ($\mu_{K(bulk)}$), bulk Nb ($\mu_{Nb(bulk)}$), and gas O_2 ($\mu_{O(gas)}$), respectively. For dopants, we suppose bulk Mo, Cr, and N_2 gas as the Mo, Cr, N reservoirs, respectively. In addition, as shown in our recent works[54,55], to form bulk $KNbO_3$ spontaneously, the minima of μ_K, μ_{Nb}, and μ_O satisfy

$$\mu_K^{min} = E(K_nNb_nO_{3n}) - E(K_{n-1}Nb_nO_{3n}), \tag{5a}$$

$$\mu_{Nb}^{min} = E(K_nNb_nO_{3n}) - E(K_nNb_{n-1}O_{3n}), \tag{5b}$$

$$\mu_O^{min} = E(K_nNb_nO_{3n}) - E(K_nNb_nO_{3n-1}), \tag{5c}$$

where $E(K_nNb_nO_{3n})$, $E(K_{n-1}Nb_nO_{3n})$, $E(K_nNb_{n-1}O_{3n})$, and $E(K_nNb_nO_{3n-1})$ are total energies of $KNbO_3$ system consisting of n primitive cells without and with a K, Nb and O vacancy, respectively. If the energies of bulk K, Nb, and gas O_2 are set as the reference zeros, namely $\triangle\mu_K = \mu_K - \mu_{K(bulk)}$, $\triangle\mu_{Nb} = \mu_{Nb} - \mu_{Nb(bulk)}$ and $\triangle\mu_O = \mu_O - \mu_{O(gas)}$, then $\triangle\mu_K^{min} \le \triangle\mu_K \le 0$, $\triangle\mu_{Nb}^{min} \le \triangle\mu_{Nb} \le 0$ and $\triangle\mu_O^{min} \le \triangle\mu_O \le 0$. Following the above constrains, we can determine the physically allowed region of the chemical potentials and the minimum defect formation energy of the doped systems.

To obtain the shift of the VBM and CBM with respect to the pure system, the correction term $\triangle V$ has to be introduced to align the reference potential in the bulk systems with defects or impurities, which is attributed to the fact that there is no existence of absolute reference for the electrostatic potential of different periodic systems and the shift in the potential caused by the defect or impurity cannot be evaluated from supercell calculations alone. There is no utilization of $\triangle V$ in the defect formation energies calculations, calculating the shifts of VBM and CBM according to the DOS and PDOS of doped systems with reference to the pure $KNbO_3$ is inseparable from the accurate correction $\triangle V$. The preferred method[56,57] getting the correction $\triangle V$ is to realign the electrostatic potential in systems with defects or impurities to the undoped system by using its realspace value at some chosen point far from the defect or doping. Here the Nb atom farthest from the doping center are chosen to align the electrostatic potentials between pure and doped systems. Therefore, the corrected Fermi energy $E_F(cor)$ and the calculated Fermi energy $E_F(cal)$ for doped systems satisfy the following relation

$$E_F(cor) = E_F(cal) - E_F(pure) + \triangle V, \tag{6}$$

where the Fermi energy $E_F(pure)$ for pure system is set as zero to facilitate discussion. The DOS and PDOS of doped systems are adjusted with respect to the corresponding $E_F(cor)$ which is measured from $E_F(pure)$. The calculated Fermi level for N doped system by using above correction

method is 0.84 eV. Other method[58,59] has also been used to ensure the energy reference levels for doped and pure systems are the same. The DOS and Fermi levels for doped systems are shifted with reference to the Fermi level of pure system so that the peaks of 5*s* states for the Nb atom farthest away from the doping center are aligned with the peaks of Nb 5*s* states in pure system, the calculated Fermi level of 0.80 eV for N monodoped system is good agreement with that calculated by the method of aligning the electrostatic potentials between pure and doped systems, which indicates that the correction method we adopted is reasonable and reliable.

To further examine whether the photocatalytic activity of $KNbO_3$ is enhanced by the (Mo,Cr)-N passivated codoping, we discuss the VBM and CBM positions with respect to the water redox potential as well as the geometric and electronic properties for pure and doped systems, since the positions of the band edges should be modified to own a suitable bandgap with band edge positions straddling the water redox level so as to sufficiently absorb visible light. The CBM and VBM positions of $KNbO_3$ could be calculated by the empirical formula[60]:

$$E_{CBM} = (\chi_K \chi_{Nb} \chi_O^3)^{1/5} - 0.5E_g + E_0, \quad (7a)$$

$$E_{VBM} = E_{CBM} + E_g, \quad (7b)$$

where E_{CBM} and E_{VBM} denote respectively the CBM and VBM potentials of $KNbO_3$, E_g is the bandgap of $KNbO_3$ and here we use the experimental value due to our calculated bandgap is a little smaller than the experimental value, E_0, which is equal to -4.5 eV for normal hydrogen electrode, denotes the scale factor relating the reference electrode redox level to the absolute vacuum scale, and the absolute electronegativities of K, Nb, and O atoms are denoted by χ_K, χ_{Nb}, and χ_O, which are 2.42, 4 and 7.54 eV[61], respectively. Of course, the CBM and VBM positions of the pure and doped systems can also be determined by calculating the work function[62]. For this, there exist detailed discussion in the literatures for the metal oxide semiconductors such as ZnO, and consequently, the positions of the band edges determined by work function is almost same as those obtained by the electronegativity[63]. Therefore, here we only present the calculated positions of the band edges determined by the electronegativity for the pure $KNbO_3$, while the CBM and VBM levels of monodoped and codoped $KNbO_3$ are determined according to the shifts of CBM and VBM with reference to pure system.

Finally, we have analyzed optical absorption spectra of doped systems as compared to that of pure system by using the HSE functional. The absorption coefficient can be derived from the real and imaginary parts of the frequency dependent complex dielectric function $\varepsilon(\omega)=\varepsilon_1(\omega)+i\varepsilon_2(\omega)$ using the following equation[64]

$$I(\omega) = \sqrt{2}\omega\sqrt{\sqrt{\varepsilon_1^2(\omega)+\varepsilon_2^2(\omega)} - \varepsilon_1(\omega)}. \quad (8)$$

The imaginary part of the dielectric function ε_2 is given by[65]

$$\varepsilon_2(\hbar\omega) = \frac{2e^2\pi}{\Omega\varepsilon_0}\sum_{k,v,c}|\langle\psi_k^c|\mathbf{u}\cdot\mathbf{r}|\psi_k^v\rangle|^2\delta(E_k^c - E_k^v - \hbar\omega), \quad (9)$$

where Ω, v, c, ω, $\mathbf{u}$, ψ_k^v and ψ_k^c are the unit-cell volume, valence bands, conduction bands, photon frequencies, the vector defining the polarization of the incident electric field, the occupied and unoccupied wave functions at point k in reciprocal space, respectively, while the real part of the dielectric function ε_1 can be obtained from imaginary part ε_2 by the Kramer-Kronig relationship[66].

$$\varepsilon_1(\omega) = 1 + \frac{2}{\pi}p\int_0^\infty \frac{\varepsilon_2(\omega')\omega'}{\omega'^2 - \omega^2}d\omega', \quad (10)$$

where p is the principal value of the integral.

3 Results and discussion

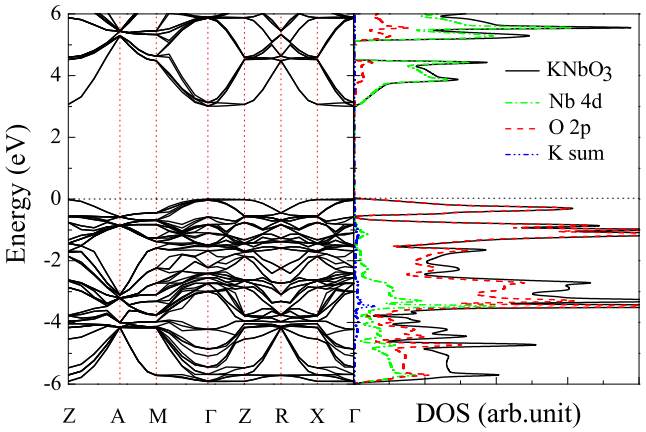

Fig. 2 Band structure (left panel), and DOS and PDOS (right panel) for pure $KNbO_3$. The black dashed lines indicate the Fermi level.

Fig.1 shows the pure $KNbO_3$ supercell with an optimized size of 8.025×8.025×8.025 Å^3 (Table 1), the Nb-O bond length is 2.006 Å and the distance between K and the adjacent O atom is 2.837 Å. Besides, the bader charge analysis in Table 2 indicates that the K, Nb, and O atoms carry charge of +0.78, +2.58, and -1.12 e, respectively. The calculated band structure and DOS are shown in Fig.2, and it can be seen that the calculated bandgap is 3.01 eV (Table 3), which is very close to

Table 1 Calculated lattice parameters, total energies and defect binding energies (E_b) for pure and doped $KNbO_3$ systems.

Systems	Lattice parameters ($Å^3$)	total energy (eV)	E_b (eV)
Pure	8.025 × 8.025× 8.025	-305.8483	-
N	8.045 × 8.033× 8.033	-303.9955	-
Mo	8.007 × 8.007× 8.007	-304.2256	-
Cr	7.974 × 7.974× 7.974	-300.6895	-
Mo-N (i)	8.151 × 7.981× 7.981	-304.7497	2.377
Mo-N (ii)	8.137 × 7.986× 7.986	-303.7449	1.372
Mo-N (iii)	8.134 × 7.991× 7.991	-303.5902	1.217
Cr-N (i)	8.146 × 7.943× 7.943	-301.7293	2.893
Cr-N (ii)	8.163 × 7.945× 7.945	-300.1066	1.270
Cr-N (iii)	8.155 × 7.946× 7.946	-299.8298	0.993

the experimental value of 3.14 eV. The top of valence band is mainly composed of O 2p states and the bottom of conduction band is contributed by Nb 4d states, while there is almost no appearance of K electronic states near the VBM and CBM, indicating that K only builds up the structure skeleton of $KNbO_3$ without affecting its electronic structure of the band edge characteristic. Therefore, doping with nonmetal atom with higher 2p orbital energy as compared to that of O atom will shift the VBM upwards and employing metal atom with lower d orbital energy as compared to the Nb 4d could decrease the CBM.

Table 2 Bader charge analysis of Nb and O atom in pure system and Mo, Cr, or N atom in doped systems. All date are in units of the number of electrons.

Systems	Nb	O	Mo	Cr	N
Pure	+2.58	-1.12	-	-	-
N	-	-	-	-	-1.14
Mo	-	-	+2.35	-	-
Cr	-	-	+1.94	-	-
Mo-N (i)	-	-	+2.30	-	-0.93
Mo-N (ii)	-	-	+2.60	-	-1.15
Mo-N (iii)	-	-	+2.58	-	-1.18
Cr-N (i)	-	-	-	+1.85	-0.72
Cr-N (ii)	-	-	-	+1.21	-1.30
Cr-N (iii)	-	-	-	+1.95	-1.17

The spin-polarization effect for the doped systems with one more or one less hole than the pure system can not be ignored, so spin-polarized calculations are adopted to treat the N, Mo, and Cr monodoped systems. Substituting one N for O atom in pure supercell to form N monodoped $KNbO_3$ will slightly increase its supercell size to 8.045×8.033×8.033 $Å^3$ (Table 1), which may be explained by the fact that the ionic radius of N ($R_{N^{3-}}$=1.46 Å) is larger compared with that of O ($R_{O^{2-}}$=1.38 Å)[67]. The Nb-N bond length of 1.981 Å is slightly shorter

Table 3 The calculated bandgaps, the shifts of VBM ($\triangle E_{VBM}$) and CBM ($\triangle E_{CBM}$), and the changes of bandgap ($\triangle E_g$) for pure and doped $KNbO_3$. The positive values indicate the increase in energy with respect to pure system. All the units are eV.

Systems	Bandgap	$\triangle E_{VBM}$	$\triangle E_{CBM}$	$\triangle E_g$
Pure	3.01	-	-	-
N	2.95	+0.05	-0.01	-0.06
Mo	2.42	+0.28	-0.31	-0.59
Cr	2.50	+0.35	-0.16	-0.51
Mo-N (i)	2.54	+0.34	-0.13	-0.47
Mo-N (ii)	1.88	+1.04	-0.09	-1.13
Mo-N (iii)	1.85	+0.87	-0.29	-1.16
Cr-N (i)	2.97	+0.33	+0.29	-0.04
Cr-N (ii)	2.63	+0.82	+0.44	-0.38
Cr-N (iii)	2.50	+0.93	+0.42	-0.51

than the original Nb-O bond length, which is attributed to the stronger coulomb interaction between N atom and the adjacent Nb atom, this can also be demonstrated by the larger charge of -1.14 e of N atom (Table 2) as compared to that of the O atom in pure $KNbO_3$. Because N atom has higher 2p orbital energy as compared to the O 2p orbital, doping with N atom will be expected to reduce the bandgap by rising up the VBM. The DOS and PDOS displayed in Fig.3(a) shows that the VBM of N monodoped $KNbO_3$ is mainly dominated by both N 2p and O 2p states, while its CBM consisting of Nb 4d states is unchanged as compared to that of pure system. Besides, its VBM rising up slightly by 0.05 eV with slightly moving downwards the CBM by only 0.01 eV results in the bandgap of 2.95 eV for N doped system (Table 3). Though the band edge positions are almost unchanged as compared to the pure system, the presence of impurity states consisting of N 2p states and O 2p states above and below the Fermi level reduce the effective bandgap of N doped system and make photoexited electron transfer from VBM to CBM require lower energy. However, just a narrower effective bandgap does not ensure satisfactory of the photocatalytic ability, the unoccupied N 2p and O 2p sates which appear above the Fermi level serving as electron-hole recombination centers may reduce the photocatalytic performance. Besides, adopting the dopant element with different chemical valence is often accompanied by defects which annihilate photogenerated charge carriers. These factors will suppress the photocatalytic efficiency of N monodoped $KNbO_3$.

Substituting one Nb atom in the center of $KNbO_3$ supercell by a Mo or Cr atom is considered to form cationic doping. The calculated results in Table 1 indicate that monodoping with Mo or Cr atom will slightly reduce the supercell size and Mo monodoped system has the smaller lattice size than Cr monodoped system, which is attributed to the cause that

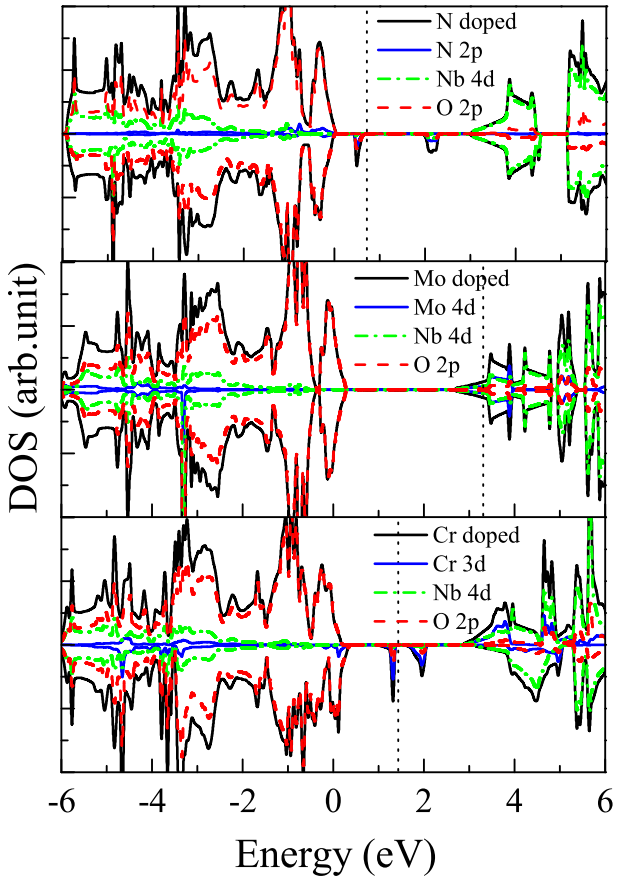

Fig. 3 DOS and PDOS for monodoped $KNbO_3$ with (a) N, (b) Mo, and (c) Cr. The Fermi level of pure $KNbO_3$ is set as energy zero. The black dashed lines represent the Fermi levels in the monodoped systems.

the ionic radius of Mo, Cr, Nb are different ($R_{Mo^{6+}}$=0.59 Å, $R_{Cr^{6+}}$=0.44 Å, $R_{Nb^{5+}}$=0.64 Å)[67]. The Mo-O bond length in Mo monodoped system and the Cr-O bond length in Cr monodoped system are respectively 1.960 and 1.916 Å, which are slightly smaller than that of original Nb-O bond length. This suggests that the Coulomb interaction between Mo (or Cr) and O atom is stronger than that between Nb and O atom. In addition, the bader charge analysis in Table 2 indicates that there exists obvious charge transfer between the Mo (or Cr) atom and the other atoms in the supercell. The DOS and PDOS of Mo monodoped system are shown in Fig.3(b), Mo monodoped system behaves as a n-type semiconductor with its Fermi level moving up to the conduction band edge. Its VBM consisting of O 2*p* states goes up by 0.28 eV and its CBM consisting of Mo 4*d* and Nb 4*d* states decreases by 0.31 eV, which result in the reduction of bandgap of 0.59 eV (Table 3). Fig.3(c) shows that the Fermi level of Cr doped system also shifts closer to

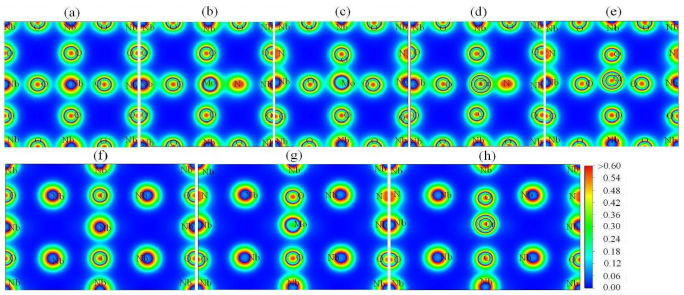

Fig. 4 Calculated electron density of pure (a),(f) and codoped systems of (b) Mo-N (i), (c) Mo-N (ii), (d) Cr-N (i), (e) Cr-N (ii), (g) Mo-N (iii) and (h) Cr-N (iii). The blue and red color regions denote the area with low and high electron density, respectively. The units are electrons $Å^{-3}$.

the conduction band edge and monodoping with Cr makes $KNbO_3$ behave as a n-type doping, which is because the Cr atom releases one more valence electron than Nb does. Cr doping introduces impurity states consisting of Cr 3*d* and O 2*p* states which do not appear in the case of Mo doping, which is mainly attributed to the fact that Cr has much lower *d* orbital energy than the Nb 4*d* orbital[28]. Though these impurity states reduce the effective bandgap, the unoccupied located states acting as electron-hole recombination centers will suppress the photocatalytic performance of Cr monodoped system. Furthermore, the created defects due to the charge imbalance promote trapping photogenerated charge carriers will also limit the photocatalytic efficiency of Mo and Cr monodoped systems.

To compensate for the charge imbalance caused by N, Mo and Cr monodoping, we consider (Mo, Cr)-N codoped $KNbO_3$. N atom is one less valence electron than O atom, while Mo or Cr atom releases one more valence electron than Nb does. Thus the incorporation of both cation Mo or Cr atom and anion N atoms passivate the adverse effects of monodoping. According to the experimental techniques such as sol-gel method or other wet chemistry methods[68], the configuration (i) for Mo-N or Cr-N codoped $KNbO_3$ which has the lowest energy (Table 1) will be obtained more easily. However, if using the synthetic procedure involving techniques such as magnetron sputtering or supersonic cluster beam deposition[69] in which the doped anions or cations are considered to be distributed among the lattice sites randomly, the situation may be different. Once the Nb atom in center of $KNbO_3$ is replaced by one Mo or Cr atom, there are 6 sites adjacent to the center atom to form codoped (i), and 12 sites in the face to form codoped (ii), and 6 sites on the edge to form codoped (iii), the probability for formation of codoped (i), (ii) and (iii) are 1/4, 1/2 and 1/4, respectively. This means that the codoped (ii) could be obtained easily and the codoped (i) and (iii) have the same opportunity to form by using magnetron sputtering

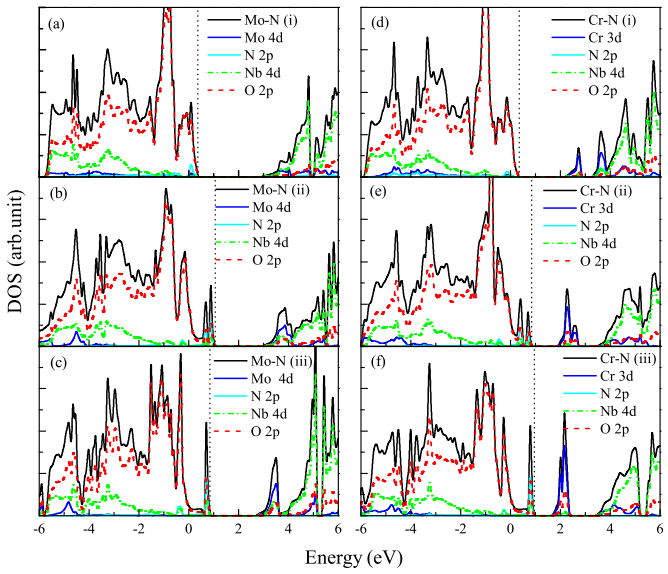

Fig. 5 DOS and PDOS for codoped systems of (a) Mo-N (i), (b) Mo-N (ii), (c) Mo-N (iii), (d) Cr-N (i), (e) Cr-N (ii), and (f) Cr-N (iii). The Fermi level of pure $KNbO_3$ is set as energy zero. The black dashed lines represent the Fermi levels for the codoped systems.

or supersonic cluster beam deposition. So we next discuss the geometry and electronic properties of all the codoped configurations. The calculated results in Table 1 show that the defect biding energies for these codoped systems are positive, which means that the Mo-N and Cr-N codoping are more favorable in energy as compared to the corresponding monodoping in $KNbO_3$ because of the strong Coulomb interaction between the dopants and the other atoms in the supercell. Furthermore, the results in Table 1 show that codoping with Mo-N or Cr-N atom pairs make the supercell expand along one direction but shrink along the other two directions. The Mo-N bond length in Mo-N codoped (i) and the Cr-N bond length in Cr-N codoped (i) are smaller than the original Nb-O bond length, which suggests the stronger Coulomb interaction between Mo (or Cr) atom and N atom than that between Nb and O atom in pure system. The electronic density displayed in Fig.4(a)(b)(d) shows that the electronic density around Mo-N or Cr-N atom pairs is larger than that around original Nb-O atom pairs. This means the electronic density between Mo (or Cr) atom and N atom in codoped systems overlaps more strongly than the overlapping of electronic density between Nb and O atom in pure system, which indicates that Mo-N or Cr-N bond has a greater covalent character as compared to that of original Nb-O bond. Seeing from the Fig.4(a-h), we can easily conclude that the dopants in all the codoped systems have the stronger covalent character than the original Nb and O atom. Besides, the bader charge analysis in Table 2 suggests that there exists obvious charge transfer between dopants and the other atoms. So we may conclude that the different Coulomb interactions between dopants and the other atoms leads to the different supercell sizes of codoped systems.

Table 4 Minimum defect formation energies (E_f) and the corresponding chemical potentials of O and Nb for doped systems. All the units are eV.

Structure	E_f	$\triangle \mu_O$	$\triangle \mu_{Nb}$
N	1.14	-4.64	0
Mo	-11.54	0	-13.91
Cr	-9.22	0	-13.91
Mo-N (i)	-8.14	0	-13.91
Mo-N (ii)	-7.13	0	-13.91
Mo-N (iii)	-6.98	0	-13.91
Cr-N (i)	-6.33	0	-13.91
Cr-N (ii)	-4.71	0	-13.91
Cr-N (iii)	-4.44	0	-13.91

We next discuss whether the different codoping positions of Mo-N and Cr-N atom pairs will obviously affect the bandgap of $KNbO_3$. For the case of Mo-N codoping, Mo-N codoped (i) has the widest bandgap of 2.54 eV with VBM rising up by 0.34 eV and CBM shifting down by 0.13 eV (Table 3), the bandgap of codoped (ii) (1.88 eV) is relatively close to the bandgap of codoped (iii) (1.85 eV). For these three codoped systems, the compositions of band edges are almost the same, i.e., the VBM is dominated by both O $2p$ and N $2p$ states, while the CBM is contributed by both Mo $4d$ and Nb $4d$ states (Fig.5(a)(b)(c)). The suitable bandgaps may make Mo-N codoped $KNbO_3$ a promising photocatalyst. Besides, we are surprised to find that Mo-N codoped system with the larger distance between Mo and N atom has the narrower effective bandgap. It can be obviously seen that the interactions between N $2p$ and O $2p$ orbitals around the Fermi levels and the interactions between Mo $4d$ and Nb $4d$, O $2p$ orbitals around CBM increase with the increase of the distance between Mo and N atom, which should be the cause of the different bandgaps of these Mo-N codoped systems. The DOS and PDOS for Cr-N codoped $KNbO_3$ are shown in Fig.5(d)(e)(f), the VBM of Cr-N codoped (i) is mainly composed of O $2p$ states, but the VBM of Cr-N codoped (ii) and (iii) are dominated by both N $2p$ and O $2p$ states. However, the CBM of all the Cr-N codoped systems are mainly contributed by Cr $3d$ and Nb $4d$ states. Some unoccupied impurity states mainly contributed by Cr $3d$ states appear between VBM and CBM, which is quiet different from the case of Mo-N codoped systems. This should be attributed to the much lower Cr d orbital energy as compared to the Mo $4d$ and Nb $4d$ orbital[28]. These unoccupied impurity states reduce the effective bandgaps, but

they may trap excite electrons resulting in the enhancement of electron-hole recombination and suppressing the photocatalytic performance.

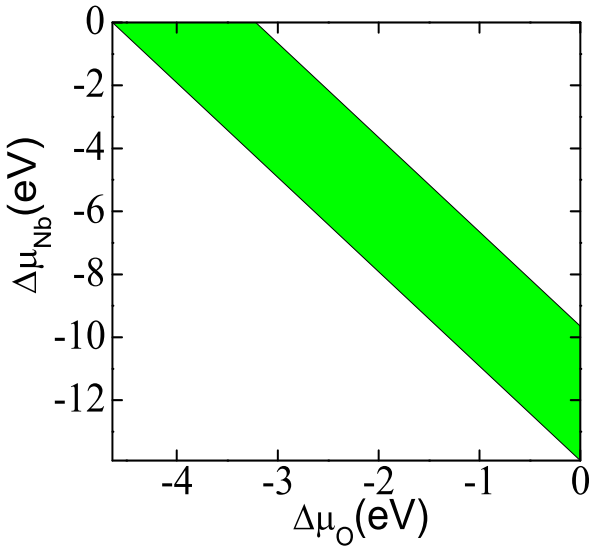

Fig. 6 The physically accessible region of the potentials in $\triangle\ \mu_O$ and $\triangle\ \mu_{Nb}$ plane for pure $KNbO_3$.

Fig.6 displays the physically accessible region of the chemical potentials for $KNbO_3$ in the $\triangle\mu_{Nb}$ and $\triangle\mu_O$ plane. In addition, the calculated defect formation energies for doped systems as a function of $\triangle\mu_{Nb}$ and $\triangle\mu_O$ are plotted in Fig.7(a-i) and the minimum defect formation energies are summarized in Table 4. For the case of N doping, the defect formation energy is found to decrease with the decrease in the chemical potentials of O atom and the minimal defect formation energy is 1.14 eV with $\triangle\mu_O$ = -4.64 eV (O-poor) and $\triangle\mu_{Nb}$ = 0 eV (Fig.7(a) and Table 4). This is attributed to the cause that the vacancy which is indispensable condition for alternative doping is easy to form under host-poor growth condition. Analogously, the defect formation energy for the case of monodoping with Mo or Cr decreases with the decline of the chemical potentials of Nb atom (Fig.8 (b) and (c) because the Nb vacancies are easy to form under Nb-poor growth condition, the minimal defect formation energies for Mo and Cr monodoped systems are -11.54 and -9.22 eV with $\triangle\mu_{Nb}$ = -13.91 eV (Nb-poor) and $\triangle\mu_O$ = 0 eV (Table 4), respectively. Besides, the minimal defect formation energy of N doped system is positive which indicates that $KNbO_3$ is difficult to be p type doped. As is shown in Fig.7(d-i), it is energetically favorable to form Mo-N or Cr-N codoped systems under O-rich and Nb-poor conditions and the defect formation energies for codoped systems are lower than that of N monodoped system, which indicates that introducing Mo or Cr atom will promote the N doping. This could be explained by the stronger Coulomb interaction between the dopants and the other atoms in the systems than that of pure system. The minimal defect formation energy for configuration (i) of Mo-N (or Cr-N) codoped system is the smallest one among all the codoped configurations, which indicates that the Mo-N (or Cr-N) atom pairs have the strongest Coulomb interaction in the codoped configuration (i).

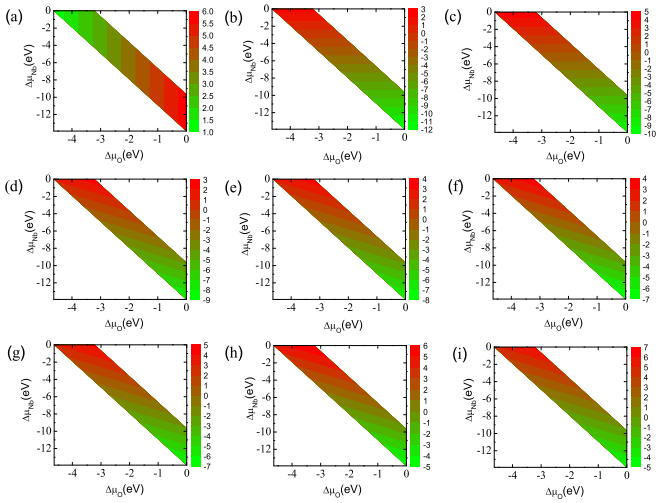

Fig. 7 The physically accessible region of the potentials in $\Delta\ \mu_O$ and $\Delta\ \mu_{Nb}$ plane for (a) N doped, (b) Mo doped, (c) Cr doped, (d) Mo-N codoped (i), (e) Mo-N codoped (ii), (f) Mo-N codoped (iii), (g) Cr-N codoped (i), (h) Cr-N codoped (ii), (i) Cr-N codoped (iii) of $KNbO_3$.

The effect of doping concentrations on the electronic structure of $KNbO_3$ is also investigated. Only Mo-N codoping reduces the bandgap to suitable value without introducing unoccupied impurity states, so here only three different Mo-N codoped configurations corresponding to the nearest, the next-nearest, and the next-next-nearest codoping with the lower doping concentration of 3.3 at% are considered. The calculated defect binding energies for Mo-N codoped (I), (II), and (III) are respectively 2.704, 1.745, and 1.614 eV, and the minimal defect formation energies for Mo-N codoped (I), (II), and (III) are respectively -8.31, -7.35, and -7.22 eV with $\triangle\mu_O$ = 0 eV (O-rich) and $\triangle\mu_{Nb}$ = -13.91 eV. The defect binding energies for Mo-N codoped (I), (II), and (III) are respectively larger than those of codoped (i), (ii), (iii), and the defect formation energies for Mo-N codoped (I), (II), and (III) are respectively smaller than those of codoped (i), (ii), (iii). This indicates that the corresponding Mo-N codoped system with the lower concentration is easier to form, and moreover, Mo-N codoped system with lower doping concentration is also more difficult to form with the increase of the distance between Mo and N atom. The calculated DOS and PDOS of Mo-N codoped (I),(II), and (III) with the doping concentration

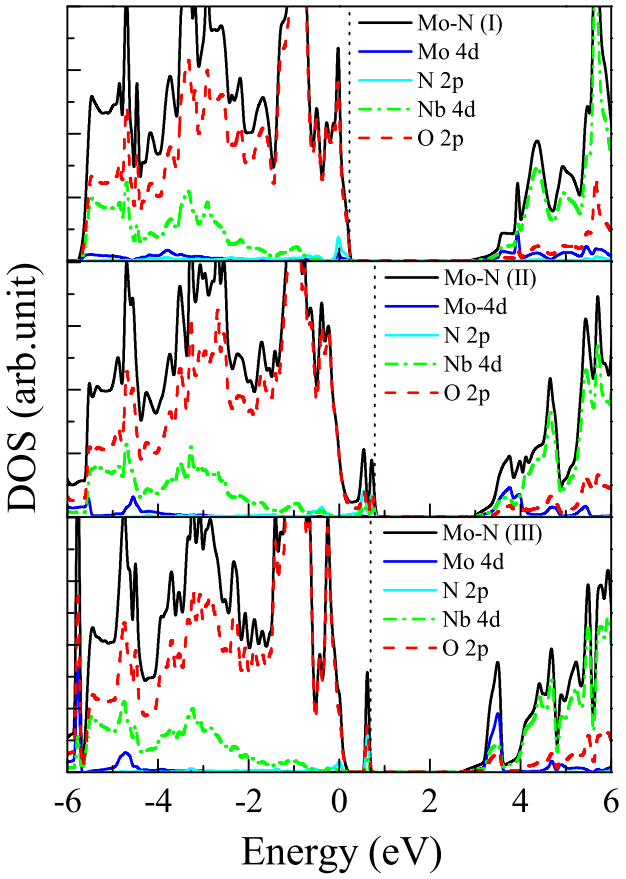

Fig. 8 DOS and PDOS for codoped systems of (a) Mo-N (I), (b) Mo-N (II), and (c) Mo-N (III). The Fermi level of pure $KNbO_3$ is set as energy zero. The black dashed lines represent the Fermi levels for the codoped systems.

of 3.3 at% are displayed in Fig.8, there are no located states between VBM and CBM of Mo-N codoped (I) and (II), but full occupied located states appear between VBM and CBM of Mo-N codoped (III). The appearance of located states of Mo-N codoped (III) may be attributed to the collective effect of large distance between Mo and N atom and the lower dopant concentration. Furthermore, the extent of the bandgap reduction is a little smaller (bandgaps for codoped (I), (II), and (III) are 2.60, 2.11, and 2.53 eV, respectively) because of lower concentration of the dopant elements. As the located states appear between VBM and CBM of Mo-N codoped (III), the effective bandgap for Mo-N codoped (III) which is the gap between the filled impurity states and the CBM is 2.00 eV. The effective bandgap for Mo-N system with lower concentration also decreases with the increase of the distance between Mo and N atom. This can also explained by the different interactions between N 2*p* and O 2*p* orbitals around the Fermi levels and the interactions between Mo 4*d* and Nb 4*d*, O 2*p* orbitals around CBM because of the different distance between Mo and N atom. In general, the appropriate effective bandgaps may make the Mo-N codoped (I), (II), and (III) suitable for visible photocatalytic decomposition of water.

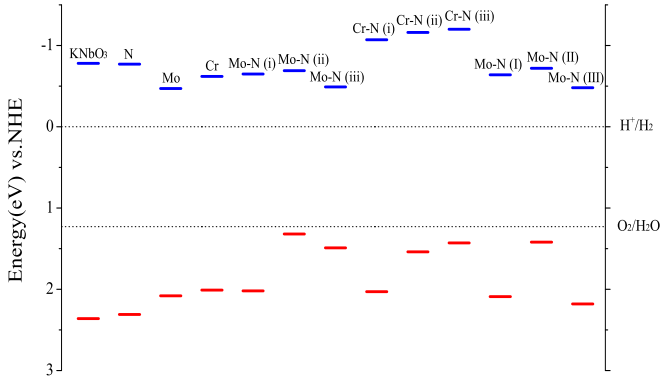

Fig. 9 Calculated VBM and CBM positions of pure, monodoped, and codoped $KNbO_3$ with respect to the water redox level. The horizontal dotted lines indicate the energy levels of redox potentials of H^+/H_2 (0 eV vs.NHE) and O_2/H_2O (1.23 eV).

Not only the bandgap but also the band edge position is important to determine the photocatalytic ability for water splitting. To assess the photocatalytic performance, we align the CBM and VBM energy levels of pure and doped systems with respect to water redox potential. The calculated CBM position of perovskite-structured $KNbO_3$ is -0.78 eV, which is agreement with the value of -0.86 eV given by Xu et al.[60], and its VBM is 2.36 eV which is calculated according to its bandgap of experimental value. Furthermore, the calculated VBM and CBM values of pure and doped systems referenced to the energy levels of water reduction potential of H^+/H_2 (0 eV versus normal hydrogen electrode, i.e., 0 eV vs. NHE) and the water oxidation potential of O_2/H_2O (1.23 eV) are illustrated in Fig.9. The VBM and CBM we discuss here are set at the the continuum band edge and the impurity states are not displayed. The band edge positions of all the monodoped and codoped systems straddle the water redox level, but the presence of unoccupied impurity states between VBM and CBM of N, Cr monodoped, and all the Cr-N codoped systems serving as electron-hole recombination centers suppress photocatalytic performance. Besides, the introduced defects due to charge imbalance trapping photogenerated charge carriers will also reduce the photocatalytic efficiency of Mo, Cr, and N monodoped systems. So Mo, Cr, N monodoped, and all the Cr-N codoped systems are unsuitable for photocatalytic water splitting under visible light. All the Mo-N codoped systems with the doping concentration of both 5.0 at% and 3.3 at% owning suitable bandgaps and band edge positions makes

them be promising for photocatalytic decomposition of water by using visible light.

As only the Mo-N codoping could make the $KNbO_3$ suitable for photocatalytic decomposition of water, so only the optical spectrum of pure and Mo-N codoped systems are calculated to confirm the better visible light absorption. The calculated optical spectrum of pure and Mo-N codoped systems with the doping concentrations of both 5.0 at% and 3.3 at% are shown in Fig.10. The absorption curve for pure $KNbO_3$ is limited to the ultraviolet region, all the Mo-N codoped systems could make use of a longer wavelength of the visible light spectrum as compared to the pure system for efficient photocatalysis. Even the absorption shifts of the Mo-N codoped (I), (II), and (III) with lower doping concentration towards to the visible light region are also quite significant. Furthermore, the next-nearest configuration have exhibited more obviously shift of optical absorption towards to the visible light region as compared to the other codoped configurations.

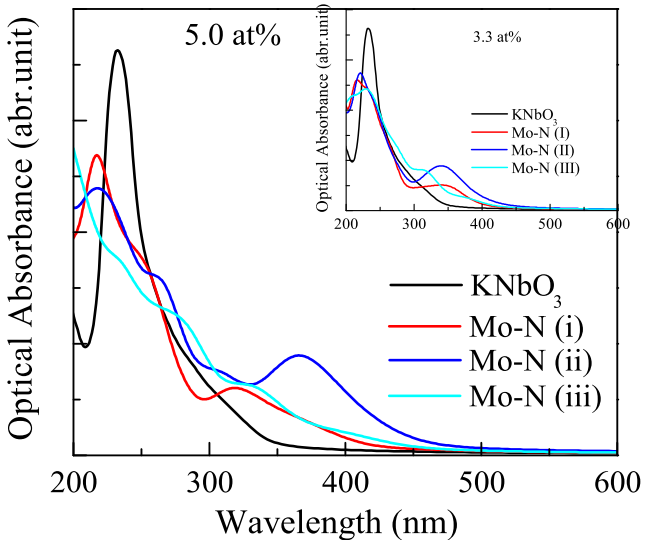

Fig. 10 The calculated absorption curves for the pure and Mo-N codoped $KNbO_3$ with the doping concentration of 5.0 at%. The insert shows the same with the doping concentration of 3.3 at%.

4 Conclusions

The first-principles calculations have been performed by using hybrid density functional to explore if monodoping with Mo, Cr, N and codoping with Mo-N, Cr-N atom pairs will improve the photocatalytic activity of $KNbO_3$. Especially, we explore the influence on the electronic structure of $KNbO_3$ caused by the codoping positions of Mo-N or Cr-N atom pairs and different doping concentrations. In addition, we choose the farthest Nb atom away from the dopants to align the electrostatic potentials of doped systems with reference to the pure system so as to correct the shift in reference level ($\triangle V$). The calculated defect formation energies show that N doped $KNbO_3$ is difficult to form, but N doping could be greatly promoted by Mo or Cr doping because of the strong Coulomb interaction between dopants and the other atoms in the system. In addition, the codoped systems with the lower dopant concentration are easier to form. Though the effective bandgaps of N, Cr monodoped, Cr-N codoped systems are reduced, the presence of unoccupied impurity states between VBM and CBM serving as recombination centers for electrons and holes suppress their photocatalytic performance. Besides, defects introduced by charge imbalance trapping photogenerated charge carriers will reduce the photocatalytic efficiency of Mo monodoped system. Though reduction of effective bandgap for Mo-N codoped system decreases with the decline in doping concentration, the optical absorption shift towards visible light region is still significant. The appropriate bandgaps and moderate positions of VBM and CBM with respect to the water redox level make the Mo-N codoped systems promising photocatalysts for water splitting under visible light.

Acknowledgments

This work was supported by the National Natural Science Foundation of China under Grant Nos. 11175146 and 10904125, the Natural Science Foundation of Chongqing under Grant Nos. CSTC-2011BA6004 and CSTC-2008BB4253 and the Fundamental Research Funds for the Central Universities under Grant Nos. XDJK2012C038, XDJK2014D044 and XDJK2015C045.

References

1 Q. Wang, Q. Sun, P. Jena and Y. Kawazoe, *Acs. Nano.*, 2009, **3**, 621-626.
2 G. Wang, H. Yuan, A. Kuang, W. Hu, G. Zhang and H. Chen, *Int. J. Hydrogen Energy*, 2014, **39**, 3780-3789.
3 K. Maeda and K. Domen, *J. Phys. Chem. C*, 2007, **111**, 7851-7861.
4 K. Maeda and K. Domen, *J. Phys. Chem. Lett.*, 2010, **1**, 2655-2661.
5 H. Tong, S. Ouyang, Y. Bi, N. Umezawa, M. Oshikiri and J. Ye, *Adv. Mater.*, 2012, **24**, 229-251.
6 N. Serpone and A. V. Emeline, *J. Phys. Chem. C*, 2012, **3**, 673-677.
7 X. Chen, S. Shen, L. Guo and S. S. Mao, *Chem. Rev.*, 2010, **110**, 6503-6570.
8 A. Fujishima and K. Honda, *Nature*, 1972, **238**, 37-38.
9 X. Zhang, J. Qin, Y. Xue, P. Yu, B. Zhang, L. Wang and R. Liu, *Sci. Rep.*, 2013, **4**, 04596.
10 D. O. Scanlon, B. J. Morgan and G. W. Watson, *Pyhs. Rev. Lett.*, 2009, **103**, 096405.
11 K. Katsumata, C. E. J. Cordonier, T. Shichi and A. Fujishima, *J. Am. Chem. Soc.*, 2009, **131**, 3856-3857.
12 Y. Su, L. Peng, J. Guo, S. Huang, L. Lv and X. Wang, *J. Phys. Chem. C*, 2014, **118**, 10728-10739.
13 H. Kato and A. Kudo, *J. Phys. Chem. B*, 2001, **105**, 4285-4292.

14 M. Ye, M. Wang, D. Zheng, N. Zhang, C. Lin and Z. Lin, *Nanoscale*, 2014, **6**,3576-3584.
15 K. Van Benthem,C. Elsässer and R. H. French, *J. Appl. Phys.*, 2001, **90**, 6156-6164.
16 S. Kim, S. Park, G. Lee, B. Han, S. Seo and J. Kim, *Int. J. Hydrogen Energy*, 2012, **37**, 16895-168902.
17 K. Sayama, H. Arakawa and K. Domen, *Catal. Today*, 1996, **28**, 175-182.
18 K. Iwashina and A. Kudo, *J. Am. Chem. Soc.*, 2011, **133**, 13272-13275.
19 P. Reunchan, N. Umezawa, S. Ouyang and J. Ye, *Phys. Chem. Chem. Phys.*, 2012, **14**, 1876-1880.
20 L. Zhang, D. Jing, L. Guo and X. Yao, *ACS Sustainable Chem. Eng.*, 2014, **2**, 1446-1452.
21 F. Cai, Y. Tang, F. Chen, Y. Yan and W. Shi, *RSC Adv.*, 2015, **5**, 21290-21296.
22 S. Pany and K. M. Parida, *ACS Sustainable Chem. Eng.*, 2014, **2**, 1429-1438.
23 X. Jiang, Y. Wang and C. Pan, *J. Am. Chem. Soc.*, 2011, **94**, 4078-4083.
24 X. Wu, S. Yin, Q. Dong and T. Sato, *Phys. Chem. Chem. Phys.*, 2013, **15**, 20633-20640.
25 M. L. Yola, T. Eren and N. Atar, *Chem. Eng. J.*, 2014, **250**, 288-294.
26 J. Tao, M. Yang, J. W. Chai, J. S. Pan, Y. P. Feng and S. J. Wang, *J. Phys. Chem. Chem.*, 2014, **118**, 994-1000.
27 J. Zhang, W. Dang, Z. Ao, S. K. Cushing and N. Wu, *Phys. Chem. Chem. Phys.*, 2015, **17**, 8994-9000.
28 Y. Gai, J. Li, S. S. Li, J. B. Xia and S. H. Wei, *Phys. Rev. Lett.*, 2009, **102**, 036402.
29 Z. Lin, A. Orlov, R. M. Lambert and M. C. Payne, *J. Phys. Chem. B*, 2005, **109**, 20948-20952.
30 W. J. Shi and S. J. Xiong, *Phys. Rev. B.*, 2011, **84**, 205210.
31 B. C. Wang, J. Nisar, B. Pathak, T. W. Kang and R. Ahuja, *Appl. Phys. Lett.*, 2012, **100**, 182102.
32 P. Liu, J. Nisar, R. Ahuja and B. Pathak, *J. Phys. Chem. C*, 2013, **117**, 5043-5050.
33 P. Liu, J. Nisar, B. Pathak and R. Ahuja, *Phys. Chem. Chem. Phys.*, 2013, **15**, 17150-17157.
34 B. Modak, K. Srinivasu and S. K. Ghosh, *J. Phys. Chem. C*, 2014, **118**, 10711-10719.
35 B. Modak, K. Srinivasu and S. K. Ghosh, *Phys. Chem. Chem. Phys.*, 2014, **16**, 17116-17124.
36 Y. Jiang, H. Yuan and H. Chen, *Phys. Chem. Chem. Phys.*, 2015, **17**, 630-637.
37 T. Zhang, K. Zhao, J. Yu, J. Jin, Y. Qi, H. Li, X. Hou and G. Liu, *Nanoscale*, 2013, **5**, 8375-8383.
38 S. Y. Ryu, J. Choi, W. Balcerski, T. K. Lee and M. R. Hoffmann, *Ind. Eng. Chem. Res.*, 2007, **46**, 7476-7488.
39 Q. P. Ding, Y. P. Yuan, X. Xiong, R. P. Li, H. B. Huang, Z. S. Li, T. Yu, Z. G. Zou and S. G. Yang, *J. Phys. Chem. C*, 2008, **112**, 18846-18848.
40 H. Shi and Z. Zou, *J. Phys. Chem. Solids*, 2012, **73**, 788-792.
41 L. Yan, J. Zhang, X. Zhou, X. Wu, J. Lan, Y. Wang, G. Liu, J. Yu and L. Zhi, *Int. J. Hydrogen Energy*, 2013, **38**, 3554-3561.
42 J. W. Liu, G. Chen, Z. H. Li and Z. G. Zhang, *Int. J. Hydrogen Energy*, 2007, **32**, 2269-2272.
43 Y. Shen and Z. Zhou, *Chem. Phys. Lett.*, 2008, **454**, 114-117.
44 R. W. Wang, Y. F. Zhu, Y. F. Qiu, C. F. Leung, J. He, G. J. Liu and T. C. Lau, *Chem. Eng. J.*, 2013, **226**, 123-130.
45 B. Wang, P. D. Kanhere, Z. Chen, J. Nisar, B. Pathak and R. Ahuja, *J. Phys. Chem. C*, 2013, **117**, 22518-22524.
46 C. Wang, H. Qiu, T. Inoue and Q. Yao, *Int. J. Hydrogen Energy*, 2014, **39**, 12507-12514.
47 G. Kresse and D. Joubert, *Phys. Rev. B*, 1999, **59**, 1758-1775.
48 G. Kresse and Furthmüller, *Phys. Rev. B*, 1996, **54**, 11169-11186.
49 M. Ernzerhof and G. E. Scuseria, *J. Chem. Phys.*, 1999, **110**, 5029-5036.
50 J. A. White and D. M. Bird, *Phys. Rev. B*, 1994, **50**, 4954-4957.
51 H. J. Monkhorst and J. D. Pack, *Phys. Rev. B*, 1976,**13**, 5188-5192.
52 J. Heyd, G. E. Scuseria and M. Ernzerhof, *J. Chem. Phys.*, 2003, **118**, 8207-8215.
53 J. Heyd, G. E. Scuseria and M. Ernzerhof, *J. Chem. Phys.*, 2006, **124**, 219906.
54 Y. Feng, X. R. Chen, T. Zhou, H. K. Yuan and H. Chen, *Appl. Surf. Sci.*, 2015, **346**, 1-10.
55 Y. Feng, T. Zhou, X. R. Chen, H. K. Yuan and H. Chen, *J. Magn. Magn. Mater.*, 2015, **387**, 118-126.
56 C. J. Van de Wallea and J. Neugebauer, *J. Appl. Phys.*, 2004, **95**, 3851-3879.
57 C. W. M. Castleton, A. Höglund and S. Mirbt, *Phys. Rev. B*, 2006, **73**, 035215.
58 J. Nisar, B. C. Wang, B. Pathak, T. W. Kang and R. Ahuja, *Appl. Phys. Lett.*, 2011, **99**, 051909.
59 B. C. Wang, J. Nisar, B. Pathak, T. W. Kang and R. Ahuja, *App. Phys. Lett.*, 2012, **100**, 182102.
60 Y. Xu and M. A. A. Schoonen, *Am. Mineral.*, 2000, **85**, 543-556.
61 R. Pearson, *Inorg. Chem.*, 1988, **27**, 734-740.
62 M. C. Toroker, D. K. Kanam, N. Alidoust, L. Y. Isseroff, P. Liao and E. A. Carter, *Phys. Chem. Chem. Phys.*, 2011, **13**, 16644-16654.
63 J. Pan, S. D. Wang, Q. Chen, J. G. Hu and J. L. Wang, *ChemPhysChem*, 2014, **15**, 1611-1618.
64 S. Saha and T. P. Sinha, *Phys. Rev. B*, 2000, **62**, 8828-8834.
65 F. H. Tian and C. B. Liu, *J. Chem. Phys. B*, 2006, **110**, 17866-17871.
66 Q. Fu, T. He, J. L. Li and G. W. Yang, *J. Appl. Phys.*, 2012, **112**, 104322.
67 R. D. Shannon, *Acta Cryst.*, 1976, **32**, 751-767.
68 W. Zhu, X. Qiu, V. Iancu, X. Q. Chen, H. Pan and W. Wang, *Phys. Rev. Lett.*, 2009, **103**, 226401.
69 A. Tkach, A. Almeida, J. A. Moreira, J. P. de la Cruz, Y. Romaguera-Barcelay and P. M. Vilarinho, *Appl. Phys. Lett.*, 2012, **100**, 192909.